

Impacts of Functional Group Substitution and Pressure on the Thermal Conductivity of ZIF-8

Penghua Ying, Jin Zhang, Xu Zhang, and Zheng Zhong*

Cite This: *J. Phys. Chem. C* 2020, 124, 6274–6283

Read Online

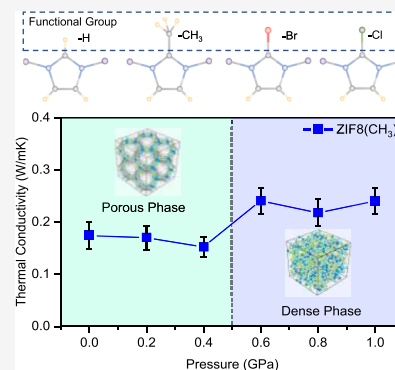
ACCESS |

Metrics & More

Article Recommendations

Supporting Information

ABSTRACT: Metal–organic frameworks (MOFs) are promising candidates as natural gas adsorbents because of their porous feature and high structural tunability. In the gas adsorption/desorption process, MOFs are often under complicated physical environments, such as varied pressure and temperature; however, limited attention has been paid to the effect of pressure on their thermal properties. In this work, taking ZIF-8 with four different functional groups (–H, –CH₃, –Cl, and –Br) as an example, we investigate the influence of functional group substitution and pressure on the thermal conductivity of MOFs through equilibrium molecular dynamics simulations. A reduction in thermal conductivity induced by the functional group substitution is observed, which is caused by a damping effect of the acoustic mismatch. Regarding the impact of pressure, the thermal conductivity of ZIF-8 is found to decrease first with increasing hydrostatic pressure. When the pressure exceeds a critical value, a sudden rise is observed in the thermal conductivity of ZIF-8 because a phase transformation from the porous phase to the dense phase is found in this process. The complicated influence of pressure on thermal conductivity is explained by a competition between the aggravation of phonon scattering and the enhancement of volumetric heat capacity in ZIF-8 with increasing pressure. This work is expected to provide molecular insights into the functional group- and pressure-dependent thermal transport of MOFs and thus facilitate their applications in energy storage and gas absorption.



1. INTRODUCTION

Metal–organic frameworks (MOFs), which are constructed from metal-based nodes bridged by coordination bonds to multidentate ligands,¹ currently are the most known porous materials.² The application potential of MOFs has attracted great interest from academia and industry³ because MOFs are crystalline materials possessing extremely large surface area and high structural tunability.⁴ Especially, MOFs can play important and critical roles in addressing today's increasing serious energy and environmental problems.^{5,6} For example, MOFs are expected to be a favorable candidate for hydrogen storage, which can facilitate the further implementation of hydrogen in fuel cell technologies.⁷ Meanwhile, a MOF material is also an excellent choice for the adsorption and separation of CO₂.⁵ However, because of their porous structure, MOFs usually have very poor thermal conductivities because the reported thermal conductivity of most MOFs is generally less than 1.0 W m⁻¹ K⁻¹.⁸ Such low thermal conductivity of MOFs will impede the removal of latent heat of adsorption in their applications of fuel cell and gas separation. In addition, the mechanism of heat transport inside MOFs is relatively unique. It is widely known that the heat can be transferred by two channels: one is the localized molecular mode (e.g., the amorphous polymer⁹) and the other is the propagating lattice mode (e.g., the crystalline solid¹⁰). Considering the abundant structures of the MOF family and its wide application in gas storage, it substantially becomes

extremely important to study the property and mechanism of thermal transport of MOFs with different framework architectures and under different physical environments (such as pressure and temperature).

The existing experiments and simulations on MOFs mainly focus on their synthesis and also applications in gas adsorption/separation, electronic devices, catalysis, and so on,¹¹ while limited attention has been paid to the heat transfer of MOFs.¹² There are only a few studies examining the thermal transport properties of some popular MOFs, such as MOF-5,^{10,13,14} ZIF-8,^{15,16} and HKUST-1.⁸ Most existing studies were carried out by molecular dynamics (MD) simulations. For example, Kavany et al. performed a pioneering computational study of the thermal conductivity of MOF-5, which was reported to be 0.31 W m⁻¹ K⁻¹ at room temperature (300 K).^{10,14} They also revealed that the molecular-mode and the lattice-mode heat currents have roughly equal contribution during the heat transport. Han et al. conducted a comprehensive investigation on the relationship between the

Received: January 22, 2020

Revised: February 25, 2020

Published: February 27, 2020

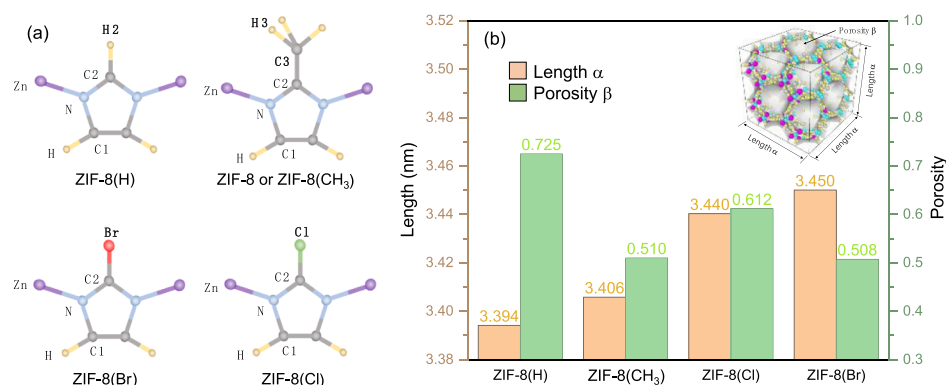


Figure 1. (a) Atomic structure and (b) structural parameters including crystal length and porosity of $2 \times 2 \times 2$ supercells of ZIF-8 with different imidazolate linkers: ZIF-8(H), ZIF-8(CH₃), ZIF-8(Br), and ZIF-8(Cl).

thermal conductivity and the framework architecture of MOF-5 including node-linker mass, shear stiffness, strain engineering, and linker arm length.¹³ A flexible force field¹⁷ was developed by Jiang's group for ZIF-8, which was successfully utilized in studying its thermal conductivity.¹⁵ The obtained thermal conductivity of ZIF-8 is $0.165 \text{ W m}^{-1} \text{ K}^{-1}$ at room temperature.¹⁵ Very recently, impacts of ethanol and water adsorptions on the thermal conductivity of ZIF-8 were reported for achieving a better understanding of the heat-transfer mechanism of MOFs with fluid adsorption.¹⁶ In addition to the realistic full-atom simulations, a series of idealized porous models were adopted by Wilmer et al. to investigate the effect of pore features (size and shape) and gas adsorption on the heat transfer in MOFs,^{18,19} which suggested that the thermal conductance can be reduced as the concentration of gas in the pores increases.

As one representative example of MOFs with high structural tunability, ZIF-8 has been widely synthesized in experiments. Although the imidazolate linker (i.e., the functional group) of the conventional ZIF-8 is CH₃, ZIF-8 materials constructed by other functional groups have been successfully synthesized recently. For example, Mortada et al. have synthesized ZIF-8(Cl) and ZIF-8(Br) by substituting the original functional group (CH₃) by Cl and Br without changing the sodalite topology.²⁰ The energetic performances, structural properties, and adsorptive properties of these ZIF-8 materials constructed by different functional groups have been investigated by Chaplais et al.²¹ Based on ab initio calculations, Dürholt et al.²⁵ developed a force field (in the MOF-FF style) for different ZIFs, which includes the conventional ZIF-8(CH₃) with a functional group of CH₃, two synthetic derivative ZIF-8 materials [ZIF-8(Br) and ZIF-8(Cl) with the functional group, respectively, being Br and Cl], and ZIF-8(H) with a functional group of H. However, to the best of our knowledge, the impact of functional group substitution on the thermal conductivity of ZIF-8 materials remains unexplored. In this study, taking four common ZIF-8 materials ZIF-8(CH₃), ZIF-8(H), ZIF-8(Br), and ZIF-8(Cl) with different functional groups as examples, we investigate the influence of the functional group of MOFs on their thermal conductivity through MD simulations. In addition, because ZIF-8 is known to exhibit a high gas adsorption capacity,^{22–24} in the present study, it is also chosen as a representative example to examine the thermal transport rule of MOFs under different pressures and temperatures in the applications of gas storage and adsorptions. It is the first time that the effects of functional group and pressure are

simultaneously considered in the study of the thermal conductivity of MOFs. It is highly expected that this study can enhance the understanding of the heat transport mechanism of MOFs with different framework architectures and pressures.

2. METHODOLOGY

2.1. Simulation Models. Four different ZIF-8 materials including the conventional ZIF-8(CH₃) and its three derivatives, that is, ZIF-8(H), ZIF-8(Br), and ZIF-8(Cl), were investigated in our research. The atomic structures of these ZIF-8 materials are shown in Figure 1a. The initial atomic structures used for MD simulations were obtained from ab initio calculations.²⁵ In our MD simulations, the interactions among atoms in ZIF-8 were described by the force field MOF-FF.²⁶ The parameters of MOF-FF implemented in our MD simulations were obtained from ref 25. It is shown in the previous study that the MD simulations together with the MOF-FF force field can properly describe the flexible property (crucial linker swing effect) of a large number of ZIF-8 derivatives and accurately predict their mechanical properties, which are comparable to the results obtained from ab initio simulations.²⁵ As plotted in Figure S1, the radial distribution of four ZIF-8 materials with different functional groups is identical to each other, which proves that different ZIF-8 derivatives share a similar skeleton structure with sodalite topology though they possess different functional groups. The $2 \times 2 \times 2$ supercells of ZIF-8 materials (see the inset of Figure 1b) with periodic boundary along three mutually perpendicular directions were adopted in our study. This treatment can efficiently exclude the boundary effect of the system, which makes the calculation results more realistic.

2.2. Thermal Conductivity Calculations. In this study, equilibrium MD simulations together with the Green–Kubo method^{27,28} were utilized to calculate the heat current autocorrelation function (HCACF), which was thus utilized to obtain the running thermal conductivity tensor $k_{\mu\nu}(t)$ ($\mu, \nu = x, y, \text{ and } z$) at a given correlation time t ²⁹

$$k_{\mu\nu}(t) = \frac{V}{k_B T^2} \int \langle J_\mu(0) J_\nu(t) \rangle dt \quad (1)$$

where k_B is Boltzmann's constant, T is the system temperature, V is the volume of the simulation box, J is the heat current, and $\langle J_\mu(0) J_\nu(t) \rangle$ represents the average HCACF over different time origins. Because the $2 \times 2 \times 2$ supercells adopted in our MD

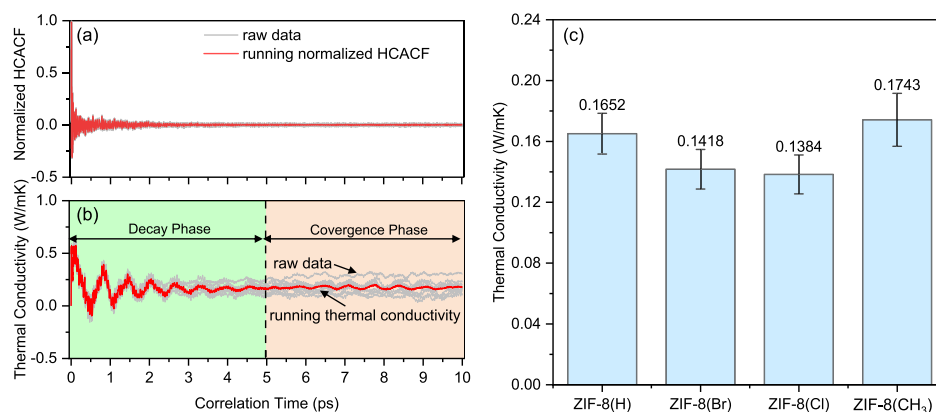


Figure 2. (a) Running normalized HCACF and (b) thermal conductivity of ZIF-8(CH₃) with increasing correlation time. Here, the running HCACF and thermal conductivity were calculated as the average value of 10 independent simulation raw data sets. (c) Thermal conductivity of ZIF-8 with different functional groups.

calculations are isotropic in three directions, eq 1 can be further simplified as

$$k(t) = \frac{V}{3k_{\text{B}}T^2} \int \langle J(0)J(t) \rangle dt \quad (2)$$

The whole MD simulation process conducted in the present study was implemented by using the publicly available simulation code LAMMPS,³⁰ in which the standard Newton equations of motion were integrated in time using the velocity Verlet algorithm. Specifically, the time step was set as 0.1 fs. During the MD simulation process, the conjugate gradient method was first adopted to perform energy minimization to ZIF-8. The obtained structures were then relaxed at 300 K and 0 GPa in the NPT ensemble (constant number of particles, pressure, and temperature) for 1 ns using the Nosé–Hoover thermostat,^{32,33} followed by another relaxation in the NVT ensemble (constant number of particles, volume and temperature) for another 1 ns. After the sufficient structural relaxation, MD simulations were performed in the NVE ensemble (constant volume without thermostat) to calculate the HCACF and the running thermal conductivity. Here, the sampling interval of HCACF calculations was every 10 steps. As shown in Figures 2b and S3, the correlation time was 10 ps for ZIF-8(H), ZIF-8(CH₃), and ZIF-8(Cl) but 20 ps for ZIF-8(Br). The different correlation time used for ZIF-8(Br) is due to the fact that the running thermal conductivity of ZIF-8(Br) needs more correlation time to reach convergence when compared to the other three ZIF-8 materials, which will be discussed later. In order to avoid the possible statistic error, 10 independent calculations were conducted to obtain the average value of the thermal conductivity. Hence, the total simulation step in the NVE ensemble was 1 million steps (corresponding to 100 ps) for ZIF-8(H), ZIF-8(CH₃), and ZIF-8(Cl) and 2 million steps (corresponding to 200 ps) for ZIF-8(Br). In simulating the ZIF-8 materials under different hydrostatic pressures, they were relaxed at 300 K and under the specific pressure in the NPT ensemble for 2 ns. Afterward, similar MD simulations in the NVE ensemble were performed to calculate the thermal conductivity of the ZIF-8 materials under the pressure. Here, six pressures (0, 0.2, 0.4, 0.6, 0.8, and 1.0 GPa) ranging from 0 to 1.0 GPa were considered in our study. It is worth noting that the heat flux calculation approach for many-body interactions in the conventional LAMMPS is uncorrected because only the two-body potentials were considered in

calculating the virial stress heat flux.^{31,32} Here, we adopted the software patch developed by Wilmer's group³² to LAMMPS, in which the correct heat flux calculation approach is implemented. The thermal conductivities of four ZIF-8 materials calculated by both corrected and uncorrected LAMMPS are compared in Figure S2. It is shown that the thermal conductivity of ZIF-8 obtained from the corrected LAMMPS is about 8.3–14.4% higher than the value achieved from its uncorrected counterpart.

3. RESULTS AND DISCUSSION

In this section, the aforementioned equilibrium MD simulations together with the Green–Kubo method were employed to study the thermal conductivity of ZIF-8 and its derivatives with different functional groups. Three different effects including functional group substitution, hydrostatic pressure, and temperature were discussed.

3.1. Functional Group Effect. The initial structure parameters including the length α (i.e., the size of the simulation box) and porosity β are plotted in Figure 1b. It is noted that the porosity was calculated through a polyhedral mesh algorithm encapsulated in the open-source OVITO package,^{33,34} in which the probe sphere radius was set as 5.0 Å. As shown in Figure 1b, ZIF-8(H) shows the largest porosity and the smallest crystal length, while ZIF-8(Br) has the smallest porosity and the largest crystal length. The different crystal lengths and porosities of different ZIF-8 materials are attributed to their different functional groups. For example, the bond length $d_{\text{C2-fg}}$ (fg = Br, Cl, CH₃, and H denoting different functional groups, C2 denoting the carbon atoms connecting the functional groups on the skeleton as plotted in Figure 1a) between the functional groups and the skeleton follows $d_{\text{C2-Br}}$ (0.189 nm) > $d_{\text{C2-Cl}}$ (0.170 nm) > $d_{\text{C2-CH}_3}$ (1.503 nm) > $d_{\text{C2-H}}$ (0.110 nm), which is consistent with the distribution of their crystal length. However, the change of porosity of ZIF-8 materials having different functional groups generally shows the opposite trend with the bond length. The longer bond length makes the void space enclosed by the constructed surface mesh much smaller. The only exception is ZIF-8(CH₃), which has a shorter bond length but a much smaller porosity than ZIF-8(Cl), which is caused by the fact that there exist three C–H bonds toward different directions in the functional group, making the porosity significantly reduced.

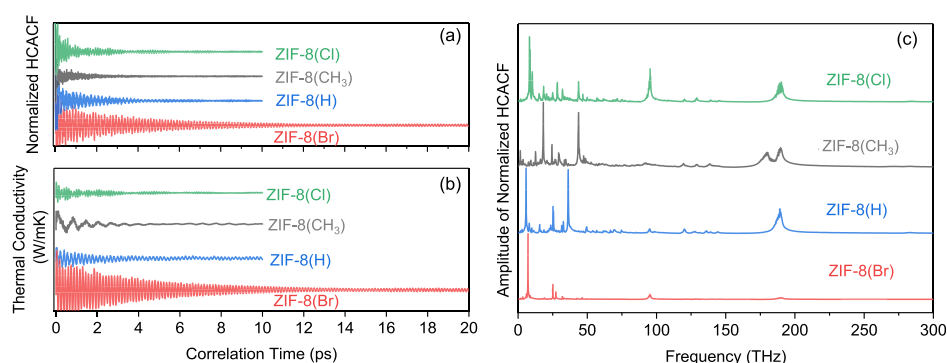


Figure 3. (a) Normalized HCACF, (b) normalized thermal conductivity, and (c) power spectrum of normalized HCACF of different ZIF-8 materials. The green, black, blue, and red lines are results of ZIF-8(Cl), ZIF-8(CH₃), ZIF-8(H), and ZIF-8(Br), respectively. In all plots, the curves are offset for clarity.

As stated above, the heat current data of every successive 10 ps in our simulations was treated as an individual sample result. By averaging sufficient sample results, we can obtain the average value of HCACF and running thermal conductivity. Taking ZIF-8(CH₃) as an example (see Figure 2a,b), its HCACF and thermal conductivity both fluctuate significantly at the early stage. However, as the simulation time increases, the fluctuation begins to decay, which finally results in the convergence of both HCACF and thermal conductivity, though the HCACF decays much faster than the thermal conductivity. From eq 1, we can clearly see that the running thermal conductivity is a function of the correlation time. Thus, in order to achieve the statistical accuracy of obtained thermal conductivity, in the present study, the thermal conductivity was obtained by averaging the value of last 5 ps at the convergence phase as plotted in Figure 2b. The evolution of HCACF and running thermal conductivity with growing correlation time of other ZIF-8 materials, that is, ZIF-8(H), ZIF-8(Cl), and ZIF-8(Br), can be found in Figure S3. The estimated thermal conductivity of the conventional ZIF-8, that is, ZIF-8(CH₃), is 0.1743 W m⁻¹ K⁻¹, which is slightly larger than the existing result of 0.165 W m⁻¹ K⁻¹ reported in previous simulation studies.^{15,16} This difference can be attributed to the following two factors. First, we used a newly developed force field MOF-FF, which is different from the conventional Amber force field¹⁷ utilized in the previous study. Second, in the present study, we employed the LAMMPS package with a correction to the calculation of heat flux, while the corrected contribution of many-body interaction to heat flux was probably ignored in the previous calculations (see Figure S2).^{15,16}

As plotted in Figure 2c, the estimated thermal conductivities of other ZIF-8 derivatives are 0.1652, 0.1418, and 0.1384 W m⁻¹ K⁻¹ for ZIF-8(H), ZIF-8(Br), and ZIF-8(Cl), respectively, which are 5.22, 18.65, and 20.60% lower than that of their conventional counterpart ZIF-8(CH₃). The lower thermal conductivity observed in three ZIF-8 derivatives is caused by the acoustic mismatch between the atom C2 and the functional group (H, Cl, and Br) because the mass of these functional groups is different from atom C2 in the skeleton (see Figure 1a), which is in contrast to the comparable atomic mass between the C3 atom in ZIF-8(CH₃) and the C2 atom in its skeleton. The lattice vibration of ZIF-8 is mainly through the Zn–N–C1(C2)–N–Zn channel, while the functional group essentially does not participate in the lattice vibration. In other words, the influence of functional groups is more likely a

damping block for the heat transport. To shed more light on the mechanism behind the influence of different functional groups, the HCACF and vibrational density of states (VDOS) of four different ZIF-8 materials are carefully compared.

In Figure 3a,b, we show the evolution of normalized HCACF and thermal conductivity, respectively, of different ZIF-8 materials with the correlation time. It is clear that among the considered four ZIF-8 materials, ZIF-8(Br) shows the slowest convergence of both HCACF and running thermal conductivity. For example, when the correlation time reaches 10 ps, the HCACF and running thermal conductivity of ZIF-8(Br) still fluctuate obviously, while the results of other three ZIF-8 materials have already converged. Thus, a double correlation time, that is, 20 ps, is required for ZIF-8(Br) to obtain a stable result of thermal conductivity. In addition, among other three ZIF-8 materials, ZIF-8(CH₃) experiences the fastest convergence of HCACF and running thermal conductivity, while the convergence of ZIF-8(Cl) is the slowest. Moreover, the power spectrum of heat current is graphically shown in Figure 3c, which was obtained by applying the Fourier transform to the obtained normalized HCACF. It is found that different functional groups have different impacts on both high- and low-frequency components of the heat current. As for the low frequency below 50 THz, the peak of three ZIF-8 derivatives is on the left of the conventional ZIF-8(CH₃). As for the high frequency, ZIF-8(Cl) has an additional peak near 100 THz, while ZIF-8(Br) has no peak above 50 THz. Generally, the power spectrum of heat current of ZIF-8(H) has a distribution closest to that of ZIF-8(CH₃), while ZIF-8(Br) has only one peak at the low-frequency region.

To further provide a microscopic insight into the function group-dependent thermal conductivity of ZIF-8, we calculated the VDOS of four different ZIF-8 materials considered. Here, the VDOS were calculated by taking the Fourier transform of the atomic velocity autocorrelation function following the below equation³⁵

$$\text{VDOS}(\nu) = \int \gamma(t) \exp(-2\pi i \nu t) dt \quad (3)$$

where ν is the frequency, i is the imaginary unit, and γ denotes the velocity autocorrelation function obtained by the following equation²⁹

$$\gamma(t) = \frac{\langle \sum_i v_i(0) \cdot v_i(t) \rangle}{\langle \sum_i v_i(0) \cdot v_i(0) \rangle} \quad (4)$$

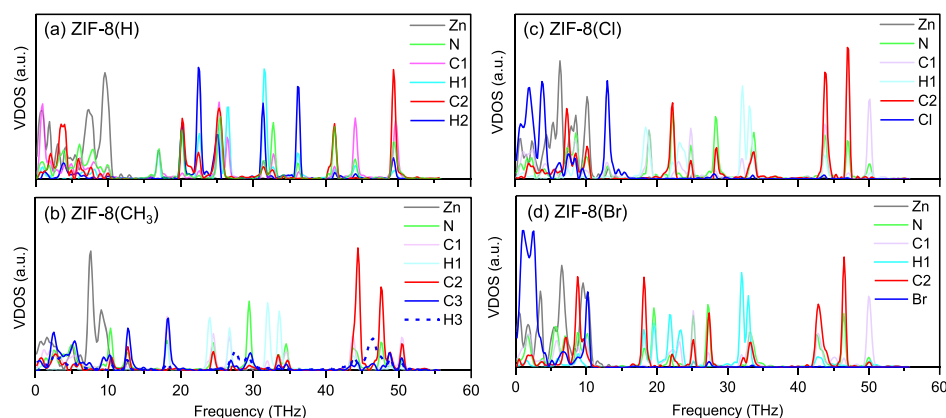


Figure 4. VDOS for the framework atoms of ZIF-8 with different functional groups: (a) ZIF-8(H), (b) ZIF-8(CH₃), (c) ZIF-8(Cl), and (d) ZIF-8(Br).

where $v_i(t)$ and $v_i(0)$ are the velocities of the i th atom at time t and the initial time, respectively.

Figure 4 shows the VDOS of the framework atoms of four ZIF-8 materials at 300 K. The atoms considered include those in the skeletons (i.e., Zn, N, C1, H1, and C2) and also the components of functional groups. It is found that in the conventional ZIF-8(CH₃), Zn only possesses the frequency between 0 and 10 THz, while the frequency of N has a wider dispersion. This observation of VDOS of the conventional ZIF-8(CH₃) is in accordance with the result reported in the previous study.¹⁵ The large gap and scant overlap between the VDOS distributions of Zn and N atoms inhibit efficient energy exchange, which thus leads to a low thermal conductivity of ZIF-8. To investigate the damping effect of imidazolate linker substitution, in this study, we turn to focus on VDOS distributions of C2 atoms (red lines in Figure 4) and the functional groups (blue lines in Figure 4). In all ZIF-8 materials, the VDOS of their C2 atoms show a wide distribution over all frequency ranges. The VDOS of four functional groups (i.e., -H, -CH₃, -Cl, and -Br) are quite different from each other. For example, the CH₃ group including C3 and H3 atoms has a VDOS distribution close to that of C2 atoms. As a result, the C2 atoms and the CH₃ group share a similar vibration frequency. When CH₃ is replaced by H, the VDOS distribution of the functional group is transferred from a wide frequency range 0–60 THz to a narrow frequency range 20–40 THz. Comparing the VDOS between H2 atoms (see Figure 4a) and C3 atoms (see Figure 4b), we can see that the peak located at 0–20 THz (for C3 atom) has leftward moved to the range of 20–40 THz (for H2 atom). This significant blue shift of high frequency is attributed to the fact that hydrogen has only 1/12 relative atomic mass compared to carbon. When CH₃ is replaced by heavy Cl or Br atoms, the VDOS distribution mainly exists at the low frequency. Specifically, the frequency of Cl is within 0–20 THz while that of Br is within 0–10 THz. The relatively atomic masses of Cl and Br are 35.5 and 79.1, which are 3.0 and 6.6 times, respectively, that of carbon atom. Comparing the atomic mass and VDOS distribution of four functional groups, we can conclude that the heavier atom has a lower frequency. However, if the atomic mass of function group is the only reason responsible for the damping effect on the heat transport of ZIF-8, it would raise a question that why ZIF-8(H) having the lightest function group possesses a lower thermal conductivity than that of ZIF-8(CH₃). This phenomenon

might be explained by the following two reasons. First, the C3 atom of the CH₃ group has the same atomic mass as that of the bonded C2 atom. As a result, they share a similar VDOS distribution (see Figure 4b), which can effectively reduce the phonon scattering. Second, as we mentioned above, the heat transport in MOFs has two channels, crystal lattice modes and localized molecular modes,^{10,13} because the configuration of MOFs is between the crystalline solid and amorphous polymers.³⁶ Thus, decreasing the mass of functional group can increase the lattice mode thermal conductivity but probably degrade the molecular mode thermal conductivity because the atom number in the functional group drops from four (CH₃) to one (H).

We further calculated the overlap energy E_{overlap} between Zn and N atoms of ZIF-8 materials with different functional groups at 300 K, which was calculated by^{15,16}

$$E_{\text{overlap}} = \int g_0(v) \frac{hv}{\exp(hv/k_B T) - 1} dv \quad (5)$$

where $g_0(v)$ is the overlap region, h is the Planck constant, v is the phonon frequency, and $1/(\exp(hv/k_B T) - 1)$ is the Bose–Einstein distribution.

As illustrated in Figure S4 in the Supporting Information, the E_{overlap} of four ZIF-8 materials has the same trend with their thermal conductivity (see Figure 2c). In other words, ZIF-8(CH₃) has the largest overlap energy, successively followed by ZIF-8(H), ZIF-8(Br), and ZIF-8(Cl). This result proves that the overlap energy between the Zn and N atoms of ZIF-8 materials has a positive correlation with their thermal conductivity, which is consistent with the results reported in previous studies.^{15,16}

3.2. Pressure Effect. As we stated above, because of their porous structure and large surface area,⁴ MOFs can be widely applied in energy storage, such as hydrogen storage and ethanol absorption. The gas absorption/desorption process inside MOFs can significantly change the pressure, which would affect the thermal transport property.³⁷ Moreover, as a material possesses a high porosity, understanding the structural stability of MOFs under a high ambient pressure is also important for MOFs in the energy storage application under complex physical environments. Here, taking the same four ZIF-8 materials, that is, ZIF-8(H), ZIF-8(CH₃), ZIF-8(Cl), and ZIF-8(Br), as typical examples, we further investigate the effect of pressure on the thermal conductivity and structural stability of MOFs, which was implemented with the aid of

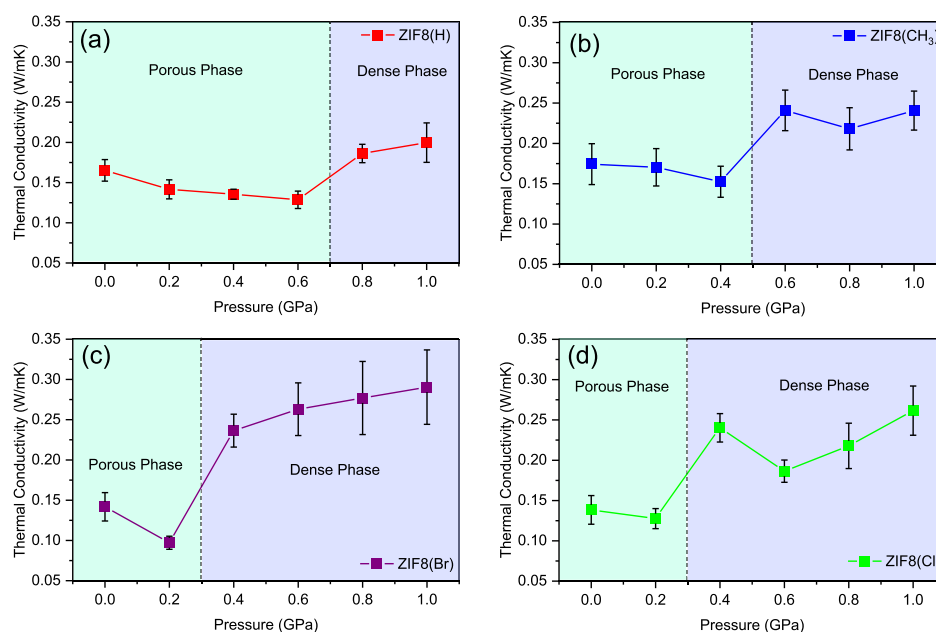


Figure 5. Thermal conductivity of ZIF-8 materials with increasing hydrostatic pressure: (a) ZIF-8(H), (b) ZIF-8(CH₃), (c) ZIF-8(Br), and (d) ZIF-8(Cl). The dash line between the porous and dense phase is taken in the middle of two critical pressures.

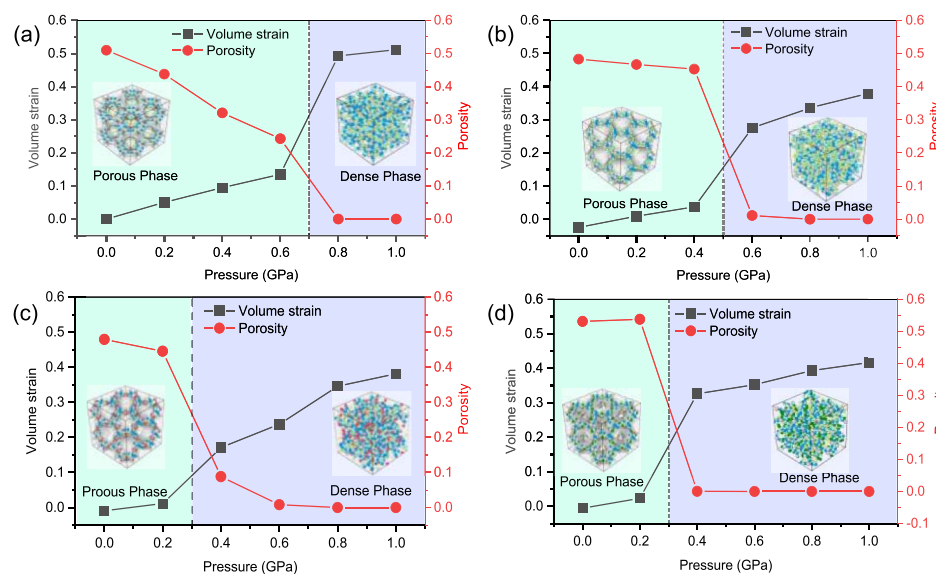


Figure 6. Change of configuration of ZIF-8 materials with increasing hydrostatic pressure: (a) ZIF-8(H), (b) ZIF-8(CH₃), (c) ZIF-8(Br), and (d) ZIF-8(Cl). The inset shows the snapshot of porous and dense phases extracted under a pressure of 0 and 1.0 GPa, respectively.

equilibrium MD simulations detailed above. Here, a certain hydrostatic pressure was applied by specifying a pressure in the *NPT* relaxation stage of the simulation.

Figure 5 shows the thermal conductivities of four ZIF-8 materials under different hydrostatic pressures ranging from 0 to 1.0 GPa. From this figure, it can be found that the thermal conductivity decreases first with increasing pressure and then encounters a sharp raise accompanied by phase transformation. Comparing with the porous crystal structure, the dense phases were observed when the pressure is greater than a certain critical value as plotted in Figure 6. The critical transformation pressure is 0.8 GPa for ZIF-8(H), 0.6 GPa for ZIF-8(CH₃), and 0.4 GPa for both ZIF-8(Cl) and ZIF-8(Br). The configurations of both porous and dense phases are plotted in Figure S5. The crystal-to-amorphous transition was found in

ZIF-8 materials when they transform from porous phase to dense phase with increasing pressure. We adopted the same algorithm and approach employed before (see Figure 1b) to calculate the change of porosity. As shown in Figure 6, the porosity of all ZIF-8 materials drops sharply to zero after the phase transformation. This phase transformation is also accompanied with a sudden change of the volume, which corresponds to an intense increase of the volume strain. It should be noted that there is an interesting phenomenon during the configuration evolution of ZIF-8 materials with increasing pressure. As shown in Figure S6, the effective volume moduli were calculated by performing the linear fitting to volume strain–pressure curves of ZIF-8 before the phase transition. It can be found that the effective volume modulus and the critical transformation pressure of ZIF-8 materials have

an opposite dependence on their functional group. The order of effective volume modulus is as follows: ZIF-8(H) < ZIF-8(CH₃) < ZIF-8(Cl) < ZIF-8(Br), which is consistent with that of their compression elastic constants and their flexible/stiff nature (ZIF-8(CH₃) and ZIF-8(Cl) are flexible while ZIF-8(Br) is stiff) reported in previous research studies.^{21,25} However, the order of critical transformation pressure of different ZIF-8 materials is as follows: ZIF-8(H) > ZIF-8(CH₃) > ZIF-8(Cl) ≈ ZIF-8(Br).

It is revealed by Coudert et al.³⁸ that the instability of a ZIF-8 material is generally induced by its shear mode softening, as the shear modulus usually decreases with increasing pressure. Inspired by this point, as plotted in Figure 7a, we calculated the

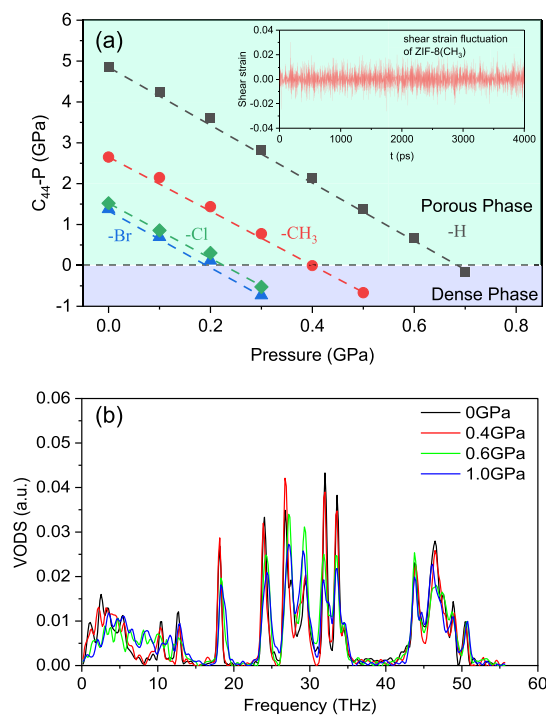


Figure 7. (a) Evolution of the stability criteria of ZIF-8 with different functional groups as a function of hydrostatic pressure. The inset shows the shear strain fluctuation of ZIF-8(CH₃) under 300 K and 0 GPa. (b) VDOS of ZIF-8(CH₃) under different pressures.

shear elastic constant C_{44} of ZIF-8 without pressure by using the strain fluctuation method (see the inset in Figure 7a).³⁹ It is found that ZIF-8(H) has a maximum C_{44} of 4.85 GPa, followed by 2.65 GPa of ZIF-8(CH₃), while ZIF-8(Cl) and ZIF-8(Br) have a much smaller C_{44} , which is only 1.52 and 1.38 GPa, respectively. When the hydrostatic pressure is applied, the shear elastic constant C_{44} of all ZIF-8 materials is found to decrease with increasing hydrostatic pressure. Specifically, the decline rates of ZIF-8(H), ZIF-8(CH₃), ZIF-8(Cl), and ZIF-8(Br) are -6.145 , -5.634 , -6.029 , and -5.819 , respectively, which were obtained by performing a linear curve fitting to the data shown in Figure 7a. These results are in good agreement with -5.57 suggested by Coudert et al.³⁸ The Born stability condition⁴⁰ for a cubic crystal under a hydrostatic pressure P , $C_{44} - P > 0$, was adopted to examine the mechanical instability of four ZIF-8 materials with different functional groups and under different pressures. As shown in Figure 7a, the phase transition (mechanical instability) of ZIF-8(Br) and ZIF-8(Cl) happens under a

pressure ranging from of 0.2 to 0.4 GPa because they have a relatively low C_{44} . However, as for ZIF-8(H) and ZIF-8(CH₃), the mechanical instability happens only when the applied pressure is in the range of 0.6–0.8 and 0.4–0.6 GPa, respectively, because they possess a much larger C_{44} . The results obtained from the mechanical instability analysis are consistent with our MD simulations, which demonstrates that the critical transformation pressure is determined by the shear stiffness of the MOFs rather than their volume modulus. This mechanism can also be utilized to explain the origin of the difference between the volume modulus and critical transformation pressure of four ZIF-8 materials (see Figure S6).

The pressure-dependent thermal conductivities of ZIF-8 materials have different trends at their porous and dense phases. At the porous phase, the thermal conductivity reduces with the increasing pressure. For example, the thermal conductivity of the conventional ZIF-8(CH₃) reduces from 0.165 to 0.129 W m⁻¹ K⁻¹ when the applied pressure increases from 0 to 0.6 GPa. Among all four ZIF-8 derivatives, ZIF(Br) is a material most sensitive to the pressure, whose thermal conductivity drops by 31.5% by applying a pressure before the onset of phase transition. This reduced thermal conductivity with increasing pressure is consistent with the results observed in other nanomaterials such as monolayer and three-dimensional graphene.^{37,41} The squeeze of ZIF-8 materials under pressure will increase the interaction among atoms, which results in a great increase of their phonon group velocity. As a result, it is thus anticipated that the pressure can increase the lattice-mode thermal conductivity. On the other hand, the volume contraction can also cause activation of soft buckling modes in the linker arms of ZIF-8 similar to that observed in the negative thermal expansion of its MOF-5 counterpart,^{41,42} which can aggravate the phonon scattering. In addition, the shear mode softening of the material caused by increasing pressure as plotted in Figure 7a could be another factor responsible for the intensified phonon scattering. Thus, the competition between the adverse effects of pressure on the phonon group velocity and the phonon scattering determines its final effect on thermal conductivity.³⁷ From the above results, we can conclude that the phonon scattering stands out in this competition.

The thermal conductivities of all four ZIF-8 materials have a sudden rise after the phase transition, leading to their thermal conductivities at the dense phase significantly larger than those at their porous phase. The largest thermal conductivity locates at the highest pressure of 1.0 GPa. Generally, compared to the ZIF-8 materials in the absence of pressure, the thermal conductivity of ZIF-8(H) and ZIF-8(CH₃) under a hydrostatic pressure of 1.0 GPa can be increased by 20.9 and 38.1%, respectively. When the same pressure of 1.0 GPa is applied, the thermal conductivity of other two ZIF-8 derivatives ZIF-8(Cl) and ZIF-8(Br) can be increased by up to 89.0 and 104.9%, respectively. Thus, it can be concluded that the thermal transport inside ZIF-8(Cl) and ZIF-8(Br) is much more sensitive to the pressure than their ZIF-8(H) and ZIF-8(CH₃) counterparts. To explain the different thermal transport behaviors of ZIF-8 before and after phase transition, taking ZIF-8(CH₃) as an example, we calculated its VDOS within the porous phase and dense phase (see Figure 7b). Here, in Figure 7b, we show four VDOS of ZIF-8(CH₃) under 0, 0.4, 0.6, and 1.0 GPa, which, respectively, correspond to the absence of pressure, the pressure just before phase transition, the pressure just after phase transition, and the maximum applied pressure.

When the applied pressure increases from 0.4 to 0.6 GPa and from 0.6 to 1.0 GPa, the intensity of phonon modes/peaks at 20–40 THz reduces significantly, which may further result in the reduction of thermal conductivity. In addition, as for the low-frequency modes (at 0–10 THz), a remarkable difference is observed between the VDOS of porous phase (0, 0.4 GPa) and dense phase (0.6, 1.0 GPa), which indicates the change in heat transport mode.

According to the kinetics theory of gases,⁴³ the thermal conductivity of crystal lattice is proportional to volumetric heat capacity. In fact, the porous structure of MOFs leads to a low volumetric heat capacity, which is an important factor responsible for its extremely low thermal conductivity. Taking ZIF-8(CH₃) as an example, we calculated its volumetric heat capacity with increasing pressure. The obtained results together with the simulation details are illustrated in the Supporting Information. It is shown in Figure S7a that, when the temperature grows from 250 to 350 K, a linear relationship is observed between the energy density E and the temperature T . Thus, the volumetric heat capacity can be calculated by performing a linear curve fitting to the obtained E – T curve. As shown in Figure S7b, no significant changes are found in the volumetric heat capacity with increasing pressure at the porous phase. However, when the pressure exceeds a critical value, the phase transition results in a great increase of volumetric heat capacity. The sharp decrease in volume and porosity of ZIF-8 materials after phase transition results in an intense increase of their volumetric heat capacity, which is the major reason for inducing the increase of thermal conductivity at the dense phase. Here, we can also find a competition mechanism between different effects of pressure on the thermal conductivity of ZIF-8. On the one hand, the applied pressure can aggravate the phonon scattering and thus reduce the thermal transport. On the other hand, the increased volume strain and porosity due to pressure can increase the volumetric specific heat, which will further enhance the heat current transportation inside the ZIF-8 materials. At the porous phase, the pressure-induced phonon scattering aggravation becomes dominant. However, after the phase transformation, the volumetric heat capacity enhancement due to the applied pressure becomes more important because the volume and porosity of ZIF-8 materials have a sudden and great reduction.

3.3. Temperature Effect. Figure 8 shows the influence of temperature on the thermal conductivity of ZIF-8 materials obtained from MD simulations. Because the ZIF-8 samples can decompose at a temperature larger than 800 K, the temperature chosen here ranges between 300 and 800 K. Generally, no evident temperature dependence is observed in the thermal conductivity of all ZIF-8 materials, which can be attributed to the fact that the relative contribution of long-range acoustic phonons is slightly dependent on temperature. Actually, a similar temperature-independent thermal conductivity is also observed in some other MOFs such as MOF-5.¹⁰ Although in a recent MD simulation study¹⁵ utilizing a different force field the thermal conductivity of ZIF-8(CH₃) is found to grow with increasing temperature, this effect of temperature is extremely small. By averaging the values of thermal conductivities under different temperatures shown in Figure 8, the thermal conductivity of different ZIF-8 materials obeys the following order: ZIF-8(CH₃) > ZIF-8(H) > ZIF-8(Cl) > ZIF-8(Br). This order is basically consistent with the results obtained at 300 K (see Figure 2b), expect that

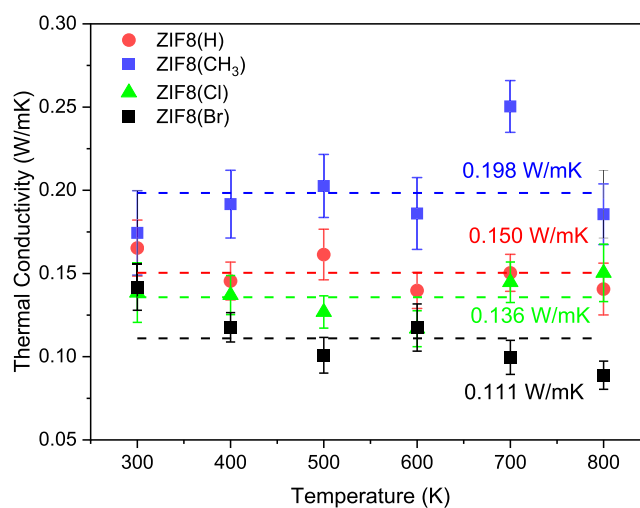


Figure 8. Thermal conductivity of ZIF-8 under different temperatures predicted by equilibrium MD simulations. The dashed line indicates the average value of thermal conductivity under different temperatures.

at 300 K ZIF-8(Br) shows a lower thermal conductivity than that of ZIF-8(Cl).

4. CONCLUSIONS

In summary, equilibrium MD simulations were performed to investigate the thermal transport properties of ZIF-8 with different functional groups. It is shown that the thermal conductivity of different ZIF-8 materials under room temperature 300 K follows the order ZIF-8(CH₃) > ZIF-8(H) > ZIF-8(Br) > ZIF-8(Cl). Specifically, the thermal conductivities of three ZIF-8 derivatives ZIF-8(H), ZIF-8(Br), and ZIF-8(Cl) are 0.1652, 0.1418, and 0.1384 W m⁻¹ K⁻¹, respectively, which is 5.22, 18.65, and 20.60% lower than that of the conventional ZIF-8(CH₃) (0.1743 W m⁻¹ K⁻¹). The reduction in the thermal conductivity of ZIF-8 induced by imidazolate linker substitution is explained by a damping effect caused by the acoustic mismatch because there exists an intense mass mismatch between the functional groups (–H, –Br, and –Cl) and the linked carbon atom in the skeleton. In addition, the dependence of thermal conductivity of ZIF-8 on pressure and temperature is also examined. It is found that when the applied pressure exceeds a critical value, ZIF-8 experiences a phase transition from the porous configuration to a dense structure. At the porous phase, as the phonon scattering plays the dominant role, the thermal conductivity of ZIF-8 decreases with increasing pressure. However, at the dense phase, the sharply reduced volume and porosity of ZIF-8 after phase transition results in an intense increase of the volumetric heat capacity, leading to the increase of thermal conductivity of ZIF-8. Specifically, the phase transition at a high pressure 1.0 GPa can increase the thermal conductivity of different ZIF-8 materials by 20.9–104.9%. The thermal conductivity of ZIF-8 is found to be independent on temperature, which is attributed to the small relative contribution of the long-range acoustic phonons. It is expected that the outcomes of this study can expand our current knowledge of heat transport mechanisms inside MOFs with different architectures and, meanwhile, provide helpful insights into the thermal controlling in future applications of MOFs, especially on gas adsorption and energy storage.

■ ASSOCIATED CONTENT


SI Supporting Information

The Supporting Information is available free of charge at <https://pubs.acs.org/doi/10.1021/acs.jpcc.0c00597>.

Radial distribution of different ZIF-8 materials; thermal conductivity of ZIF-8 materials extracted from corrected and uncorrected LAMMPS; normalized HCACF and thermal conductivity of ZIF-8(H), ZIF-8(Br), and ZIF-8(Cl) with increasing correlation time; overlap energy between Zn and N atoms of ZIF-8 materials; atomic configurations of porous and dense phases of ZIF-8 materials; effective volume modulus and transform pressure of different ZIF-8 materials; and volumetric heat capacity of ZIF-8(CH₃) under different pressures (PDF)

■ AUTHOR INFORMATION

Corresponding Author

Zheng Zhong – School of Science, Harbin Institute of Technology, Shenzhen 518055, PR China;  orcid.org/0000-0001-5293-7098; Email: zhongzheng@hit.edu.cn

Authors

Penghua Ying – School of Science, Harbin Institute of Technology, Shenzhen 518055, PR China

Jin Zhang – School of Science, Harbin Institute of Technology, Shenzhen 518055, PR China

Xu Zhang – School of Science, Harbin Institute of Technology, Shenzhen 518055, PR China

Complete contact information is available at: <https://pubs.acs.org/doi/10.1021/acs.jpcc.0c00597>

Author Contributions

P.Y. and J.Z. contributed equally.

Notes

The authors declare no competing financial interest.

■ ACKNOWLEDGMENTS

This study was supported by the National Key R&D Program of China (no. 2018YFB1502600) and the National Natural Science Foundation of China (nos. 11932005, 11772106, and 11602074).

■ REFERENCES

- (1) Zhou, H.-C. J.; Kitagawa, S. Metal–Organic Frameworks (MOFs). *Chem. Soc. Rev.* **2014**, *43*, 5415–5418.
- (2) Yaghi, O. M.; O’Keeffe, M.; Ockwig, N. W.; Chae, H. K.; Eddaoudi, M.; Kim, J. Reticular synthesis and the design of new materials. *Nature* **2003**, *423*, 705–714.
- (3) Furukawa, H.; Müller, U.; Yaghi, O. M. “Heterogeneity within order” in metal-organic frameworks. *Angew. Chem., Int. Ed. Engl.* **2015**, *54*, 3417–3430.
- (4) Burtch, N. C.; Heinen, J.; Bennett, T. D.; Dubbeldam, D.; Allendorf, M. D. Mechanical Properties in Metal–Organic Frameworks: Emerging Opportunities and Challenges for Device Functionality and Technological Applications. *Adv. Mater.* **2018**, *30*, No. e1704124.
- (5) Al-Rowaili, F. N.; Jamal, A.; Ba Shammakh, M. S.; Rana, A. A Review on Recent Advances for Electrochemical Reduction of Carbon Dioxide to Methanol Using Metal–Organic Framework (MOF) and Non-MOF Catalysts: Challenges and Future Prospects. *ACS Sustainable Chem. Eng.* **2018**, *6*, 15895–15914.

(6) Davis, S. J.; Caldeira, K.; Matthews, H. D. Future CO₂ Emissions and Climate Change from Existing Energy Infrastructure. *Science* **2010**, *329*, 1330–1333.

(7) Ren, J.; Langmi, H. W.; North, B. C.; Mathe, M. Review on processing of metal-organic framework (MOF) materials towards system integration for hydrogen storage. *Int. J. Energy Res.* **2015**, *39*, 607–620.

(8) Wieme, J.; Vandenbrande, S.; Lamaire, A.; Kapil, V.; Vanduyfhuys, L.; Van Speybroeck, V. Thermal Engineering of Metal–Organic Frameworks for Adsorption Applications: A Molecular Simulation Perspective. *ACS Appl. Mater. Interfaces* **2019**, *11*, 38697–38707.

(9) Maurin, G.; Serre, C.; Cooper, A.; Férey, G. The new age of MOFs and of their porous-related solids. *Chem. Soc. Rev.* **2017**, *46*, 3104–3107.

(10) Huang, B. L.; McGaughey, A. J. H.; Kaviany, M. Thermal conductivity of metal-organic framework 5 (MOF-5): Part I. Molecular dynamics simulations. *Int. J. Heat Mass Transfer* **2007**, *50*, 393–404.

(11) Wu, G.; Huang, J.; Zang, Y.; He, J.; Xu, G. Porous Field-Effect Transistors Based on a Semiconductive Metal–Organic Framework. *J. Am. Chem. Soc.* **2017**, *139*, 1360–1363.

(12) Luo, Y.; Ahmad, M.; Schug, A.; Tsotsalis, M. Rising Up: Hierarchical Metal–Organic Frameworks in Experiments and Simulations. *Adv. Mater.* **2019**, *31*, No. e1901744.

(13) Han, L.; Budge, M.; Alex Greaney, P. Relationship between thermal conductivity and framework architecture in MOF-5. *Comput. Mater. Sci.* **2014**, *94*, 292–297.

(14) Huang, B. L.; Ni, Z.; Millward, A.; McGaughey, A. J. H.; Uher, C.; Kaviany, M.; Yaghi, O. Thermal conductivity of a metal-organic framework (MOF-5): Part II. Measurement. *Int. J. Heat Mass Transfer* **2007**, *50*, 405–411.

(15) Zhang, X.; Jiang, J. Thermal Conductivity of Zeolitic Imidazolate Framework-8: A Molecular Simulation Study. *J. Phys. Chem. C* **2013**, *117*, 18441–18447.

(16) Wei, W.; Huang, J.; Li, W.; Peng, H.; Li, S. Impacts of Ethanol and Water Adsorptions on Thermal Conductivity of ZIF-8. *J. Phys. Chem. C* **2019**, *123*, 27369–27374.

(17) Hu, Z.; Zhang, L.; Jiang, J. Development of a force field for zeolitic imidazolate framework-8 with structural flexibility. *J. Chem. Phys.* **2012**, *136*, 244703.

(18) Babaei, H.; Wilmer, C. E. Mechanisms of Heat Transfer in Porous Crystals Containing Adsorbed Gases: Applications to Metal–Organic Frameworks. *Phys. Rev. Lett.* **2016**, *116*, 025902.

(19) Babaei, H.; McGaughey, A. J. H.; Wilmer, C. E. Effect of pore size and shape on the thermal conductivity of metal-organic frameworks. *Chem. Sci.* **2017**, *8*, 583–589.

(20) Mortada, B.; Chaplais, G.; Veremeienko, V.; Nouali, H.; Marichal, C.; Patarin, J. Energetic Performances of ZIF-8 Derivatives: Impact of the Substitution (Me, Cl, or Br) on Imidazolate Linker. *J. Phys. Chem. C* **2018**, *122*, 3846–3855.

(21) Chaplais, G.; Fraux, G.; Paillaud, J.-L.; Marichal, C.; Nouali, H.; Fuchs, A. H.; Coudert, F.-X.; Patarin, J. Impacts of the Imidazolate Linker Substitution (CH₃, Cl, or Br) on the Structural and Adsorptive Properties of ZIF-8. *J. Phys. Chem. C* **2018**, *122*, 26945–26955.

(22) Kumari, G.; Jayaramulu, K.; Maji, T. K.; Narayana, C. Temperature induced structural transformations and gas adsorption in the zeolitic imidazolate framework ZIF-8: A Raman study. *J. Phys. Chem. A* **2013**, *117*, 11006–11012.

(23) Song, Q.; Nataraj, S. K.; Roussanova, M. V.; Tan, J. C.; Hughes, D. J.; Li, W.; Bourgoïn, P.; Alam, M. A.; Cheetham, A. K.; Al-Muhtaseb, S. A.; Sivaniah, E. Zeolitic imidazolate framework (ZIF-8) based polymer nanocomposite membranes for gas separation. *Energy Environ. Sci.* **2012**, *5*, 8359–8369.

(24) Huang, H.; Zhang, W.; Liu, D.; Liu, B.; Chen, G.; Zhong, C. Effect of temperature on gas adsorption and separation in ZIF-8: A combined experimental and molecular simulation study. *Chem. Eng. Sci.* **2011**, *66*, 6297–6305.

(25) Dürholt, J. P.; Fraux, G.; Coudert, F.-X.; Schmid, R. Ab Initio Derived Force Fields for Zeolitic Imidazolate Frameworks: MOF-FF for ZIFs. *J. Chem. Theory Comput.* **2019**, *15*, 2420–2432.

(26) Bureekaew, S.; Amirjalayer, S.; Tafipolsky, M.; Spickermann, C.; Roy, T. K.; Schmid, R. MOF-FF - A flexible first-principles derived force field for metal-organic frameworks. *Phys. Status Solidi B* **2013**, *250*, 1128–1141.

(27) Green, M. S. Markoff Random Processes and the Statistical Mechanics of Time-Dependent Phenomena. II. Irreversible Processes in Fluids. *J. Chem. Phys.* **1954**, *22*, 398–413.

(28) Kubo, R. Statistical-Mechanical Theory of Irreversible Processes. I. General Theory and Simple Applications to Magnetic and Conduction Problems. *J. Phys. Soc. Jpn.* **1957**, *12*, 570–586.

(29) Haile, J. M.; Johnston, I.; Mallinckrodt, A. J.; McKay, S. Molecular dynamics simulation: elementary methods. *Comput. Phys.* **1993**, *7*, 625.

(30) Plimpton, S. Fast Parallel Algorithms for Short-Range Molecular Dynamic. *J. Comput. Phys.* **1995**, *117*, 1–19.

(31) Fan, Z.; Pereira, L. F. C.; Wang, H.-Q.; Zheng, J.-C.; Donadio, D.; Harju, A. Force and heat current formulas for many-body potentials in molecular dynamics simulations with applications to thermal conductivity calculations. *Phys. Rev. B: Condens. Matter Mater. Phys.* **2015**, *92*, 94301.

(32) Boone, P.; Babaei, H.; Wilmer, C. E. Heat Flux for Many-Body Interactions: Corrections to LAMMPS. *J. Chem. Theory Comput.* **2019**, *15*, 5579–5587.

(33) Stukowski, A. Computational Analysis Methods in Atomistic Modeling of Crystals. *J. Occup. Med.* **2014**, *66*, 399–407.

(34) Stukowski, A. Visualization and analysis of atomistic simulation data with OVITO—the Open Visualization Tool. *Modell. Simul. Mater. Sci. Eng.* **2010**, *18*, 015012.

(35) Dickey, J. M.; Paskin, A. Computer Simulation of the Lattice Dynamics of Solids. *Phys. Rev.* **1969**, *188*, 1407–1418.

(36) Han, L. Engineering Smart Thermal Properties in Metal-Organic-Frameworks. Ph.D. Thesis, University of California, 2018.

(37) Wei, Z.; Yang, F.; Bi, K.; Yang, J.; Chen, Y. Thermal transport properties of all-sp² three-dimensional graphene: Anisotropy, size and pressure effects. *Carbon* **2017**, *113*, 212–218.

(38) Ortiz, A. U.; Boutin, A.; Fuchs, A. H.; Coudert, F.-X. Investigating the Pressure-Induced Amorphization of Zeolitic Imidazolate Framework ZIF-8: Mechanical Instability Due to Shear Mode Softening. *J. Phys. Chem. Lett.* **2013**, *4*, 1861–1865.

(39) Parrinello, M.; Rahman, A. Strain fluctuations and elastic constants. *J. Chem. Phys.* **1982**, *76*, 2662–2666.

(40) Morris, J. W.; Krenn, C. R. The internal stability of an elastic solid. *Philos. Mag. A* **2000**, *80*, 2827–2840.

(41) Li, X.; Maute, K.; Dunn, M. L.; Yang, R. Strain effects on the thermal conductivity of nanostructures. *Phys. Rev. B: Condens. Matter Mater. Phys.* **2010**, *81*, 245318.

(42) Lock, N.; Christensen, M.; Wu, Y.; Peterson, V. K.; Thomsen, M. K.; Piltz, R. O.; Ramirez-Cuesta, A. J.; McIntyre, G. J.; Norén, K.; Kutteh, R.; Kepert, C. J.; Kearley, G. J.; Iversen, B. B. Scrutinizing negative thermal expansion in MOF-5 by scattering techniques and ab initio calculations. *Dalton Trans.* **2013**, *42*, 1996–2007.

(43) Kittel, C. *Introduction to Solid State Physics*, 8th ed.; John Wiley & Sons, Inc., 2004.